MATERIALS SCIENCE

Nanoarchitected metal/ceramic interpenetrating phase composites

Jens Bauer[1]†, Martí Sala-Casanovas[2]†, Mahsa Amiri[1], Lorenzo Valdevit[1,2]*

Architected metals and ceramics with nanoscale cellular designs, e.g., nanolattices, are currently subject of extensive investigation. By harnessing extreme material size effects, nanolattices demonstrated classically inaccessible properties at low density, with exceptional potential for superior lightweight materials. This study expands the concept of nanoarchitecture to dense metal/ceramic composites, presenting co-continuous architectures of three-dimensional printed pyrolytic carbon shell reinforcements and electrodeposited nickel matrices. We demonstrate ductile compressive deformability with elongated ultrahigh strength plateaus, resulting in an extremely high combination of compressive strength and strain energy absorption. Simultaneously, property-to-weight ratios outperform those of lightweight nanolattices. Superior to cellular nanoarchitectures, interpenetrating nanocomposites may combine multiple size-dependent characteristics, whether mechanical or functional, which are radically antagonistic in existing materials. This provides a pathway toward previously unobtainable multifunctionality, extending far beyond lightweight structure applications.

INTRODUCTION

Thinking beyond conventional material design methods, nanoarchitected materials (*1*) are structured from sophisticated small-scale three-dimensional (3D) designs, such as lightweight truss lattices, which allow them to harness extreme material size effects. Nanolattices have recently demonstrated several classically inaccessible properties, e.g., mechanical strength exceeding that of state-of-the-art engineering materials at a fraction of their weight. With the prospect of developing a superior future generation of high-performance lightweight materials, nanoarchitecture approaches are currently extensively studied within cellular metals (*2*–*4*) and ceramics (*5*–*8*). However, the approach is unexplored in dense materials, such as metal-ceramic composites. In general, composites may be considered the most advanced class of solids and are often the material of choice for the most demanding engineering applications, from rocket engine parts (*9*) to medical implants (*10*). In composites, the arrangement of several dissimilar materials combines many attractive characteristics, from high strength and toughness to wear and fatigue resistance, thermal stability, and biocompatibility (*11*), resulting in performance that is superior to that of the individual constituents. Expanding the concept of nanoarchitecture of materials beyond cellular metals and ceramics, this study introduces nanoarchitected metal/ceramic interpenetrating phase composites (IPCs).

Opposed to classical discontinuous particle-, fiber-, or lamellar-reinforced composites, IPCs are composed of two or multiple solid phases, each forming completely interconnected self-supporting 3D networks (*12*). Over the past two decades, extensive research on conventional (i.e., nonarchitected) metal/ceramic IPCs has demonstrated the continuity of each constituent as key for multiple beneficial properties (*13*). Mechanically, the 3D interpenetrating structure is an efficient toughening strategy (*14*–*16*), preventing crack propagation along a path of least resistance, such as only within the weaker matrix phase. The 3D interconnected reinforcement further grants IPCs improved internal load transfer over discontinuous particle-reinforced composites with the same constituents and volume fractions, thus enabling increased strength and stiffness while retaining the same ability to be designed as fully isotropic (*17*, *18*). Compared to state-of-the-art fiber- and lamellar-reinforced composites (*19*, *20*), whose properties rapidly degrade when not loaded under a preferred orientation, IPCs exceed both their out-of-plane strength and stiffness and their in-plane toughness.

Although IPCs are natural candidates for advanced 3D designs, such as beam, shell, and plate lattices, manufacturing constraints have, so far, limited these complex reinforcement topologies to macroscopic polymer/polymer pairings (*19*, *21*–*23*), with nearly no demonstration of metal/ceramic systems or at small scale. While a small number of studies have shown additively manufactured metal/ceramic IPCs (*24*, *25*), the fabrication process limited the reinforcement topology to simple millimeter-scale woodpile designs. The reported woodpile Al/Al_2O_3 IPCs (*24*) did not reach the mechanical properties of stochastic Al/Al_2O_3 IPCs with much finer features, which results in smaller flaws and higher strength. In addition, stress concentrations at the sharp reinforcement lattice nodes were identified to promote early failure. In polymeric IPCs, triply periodic minimal surface (TPMS) reinforcements (*21*–*23*, *26*) demonstrated increased stiffness, strength, and toughness over periodic beam-based architectures and stochastic nonminimal surface reinforcements. TPMS topologies, such as gyroid surfaces, are smoothly interconnected 3D shells with zero mean curvature and negative Gaussian curvature at any given point. When stressed, these topological features grant a highly uniform strain distribution, with substantially reduced stress concentrations compared to beam-based architectures while enabling similarly high strength and stiffness. Spinodal shell topologies are stochastic minimal surfaces with similar topologies and comparably beneficial properties (*27*–*29*) to TPMSs. They correspond to the 3D phase interface that is formed during spinodal decomposition (*30*, *31*) of a mixture of insoluble components. Hence, they are synthesizable via scalable self-assembly routes (*32*, *33*) and, unlike TPMS reinforcements, do not necessarily rely on additive manufacturing techniques.

[1]Materials Science and Engineering Department, University of California, Irvine, Irvine, CA 92697, USA. [2]Mechanical and Aerospace Engineering Department, University of California, Irvine, Irvine, CA 92697, USA.
*Corresponding author. Email: valdevit@uci.edu
†These authors contributed equally to the work.

RESULTS

While manufacturing complexity at small scale has limited metal and ceramic nanoarchitectures to cellular monomaterial designs, we demonstrate here a fabrication route to synthesize dense nanoarchitected metal-ceramic IPCs (Fig. 1). We used two-photon polymerization direct laser writing (TPP-DLW) 3D printing and subsequent pyrolysis to manufacture nanoscale carbon reinforcement phases with minimal surface topologies with shell thicknesses of 200 nm (Fig. 1, A and B). Subsequently, the reinforcement phases were infiltrated with nickel matrices by room temperature electrodeposition (Fig. 1C), which efficiently avoided obstacles associated with the most commonly applied high-temperature melt infiltration of metal matrices, such as residual stresses stemming from expansion mismatch between reinforcement and matrix (*34*, *35*). During deposition, the electrical conductivity of the pyrolytic carbon was exploited to initiate growth of the metal phase directly on the reinforcement surfaces. This enabled near-complete infiltration of the complexly curved nanotopologies in a single step, which has been verified via microscopy of focused ion beam (FIB)–prepared cross sections (fig. S2A). However, it is noted that because of common variability in the procedure's success rate, residual porosity may not be fully excluded and has been found in some specimens (fig. S2B). In contrast to the presented technique, reported approaches to electrodeposit cellular metallic architectures (*4*, *36*) require fabrication of a sacrificial negative template, which is then infiltrated from a conductive substrate and subsequently needs to be removed. Synthesis of minimal surface topologies has not been accomplished with this conventional route, which would require more complicated multistep processes for composite fabrication.

We systematically characterized nickel/carbon IPCs with nanoarchitected gyroid and spinodal minimal surface shell reinforcements via in situ uniaxial compression (Fig. 2). We chose the gyroid surface for being one of the most widely studied TPMS architectures. The spinodal surface was selected as a representative of a design that can be manufactured via self-assembly in a scalable way. Nickel/carbon volume ratios in the range of 80/20 to 50/50 were manufactured by adjusting the specimen sizes between 18 and 6 μm while keeping their reinforcement shell thicknesses constant at 200 nm (Fig. 2A). Figure 2B shows the IPCs' absorbed strain energy, *U*, i.e., the areas under the recorded stress-strain curves, which is a measure of their compressive toughness; the compressive strength, σ; and the Young's modulus, *E*. The shown strength and modulus rule-of-mixture bounds are predictions that were calculated from measured average properties and standard deviations (SDs) of separately compressed electrodeposited nickel and TPP-DLW–derived pyrolytic carbon micropillars (see Supplementary Text and fig. S1 for details). Figure 2C shows the engineering stress-strain response of a 52/48 gyroid IPC, which is complemented by a rule-of-mixture prediction, as computed from characteristic responses of the pure nickel and carbon (Fig. 2D). Postcompression images of all IPCs are shown in fig. S3.

Our nanoarchitected nickel/carbon IPCs demonstrated both extreme compressive strength and strain energy absorption, which, in some cases, outperformed those of both their monolithic constituents (Fig. 2B). For high metal contents, the IPCs' properties laid between or below those of their monolithic constituent solids, but they continuously increased with growing carbon fraction. Eventually, the absorbed strain energy and the strength notably exceeded the values of the constituent solids and the corresponding rule of mixture, respectively. The 52/48 gyroid IPC with the highest investigated carbon content absorbed almost five and two times as much strain energy as the monolithic carbon and nickel, respectively. Simultaneously, it sustained stresses as high as 3.5 GPa, which is 1.5 GPa stronger than the pure nickel and within the compressive strength range of the monolithic carbon. Despite being composed of almost

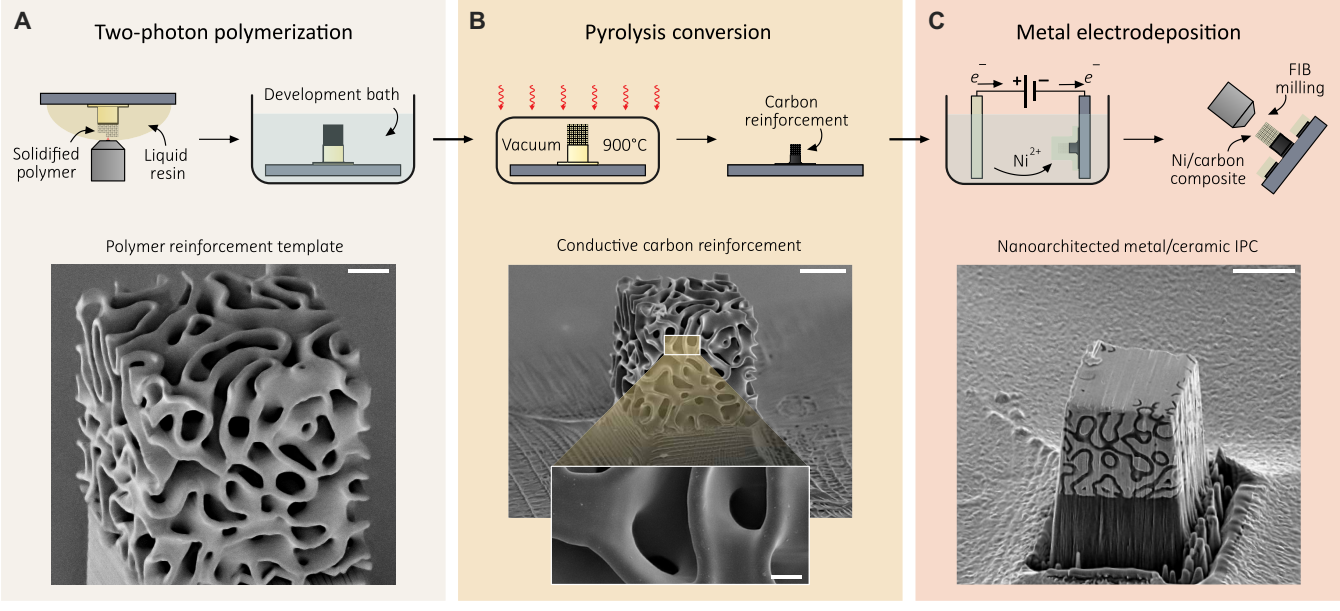

Fig. 1. Fabrication route creating nanoarchitected metal/ceramic IPCs. (**A**) TPP-DLW prints polymer-reinforcement templates with minimal surface topologies. (**B**) Accompanied by ~80% linear isotropic shrinkage, pyrolysis transforms the templates into electrically conductive carbon structures composed of 200-nm-thin shells. (**C**) Electrodeposition conformally grows nickel matrices into the carbon reinforcements; FIB milling removes excess metal on the specimen surface. Scale bars, 5 μm (overviews) and 500 nm [inset in (B)].

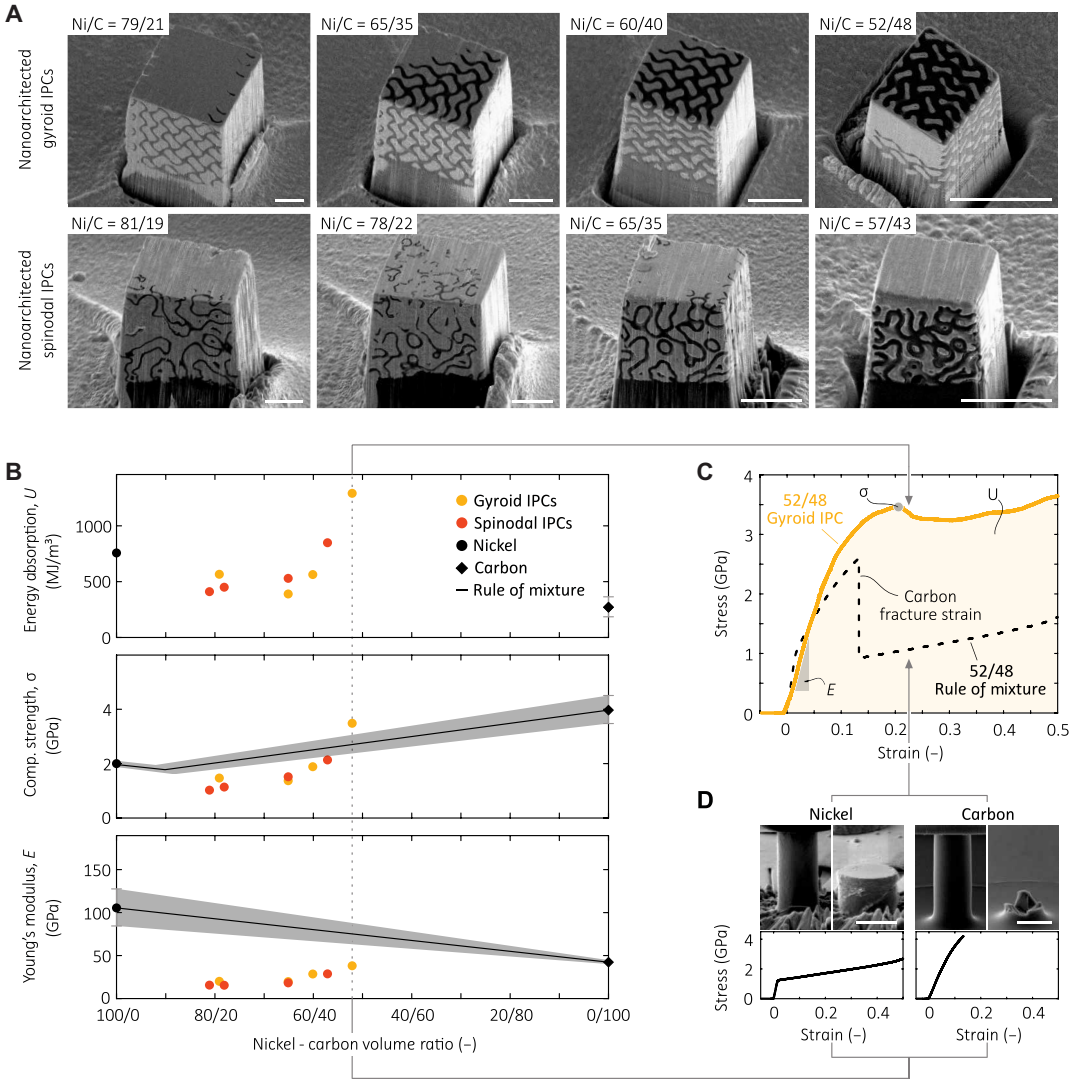

Fig. 2. Uniaxial compression experiments of nanoarchitected nickel/carbon IPCs. (**A**) Gyroid and spinodal reinforced specimens with different nickel/carbon (Ni/C) volume ratios. (**B**) Mechanical properties of the IPCs versus their nickel/carbon volume ratios compared to the average properties and standard deviations of the pure nickel and carbon data and derived rule-of-mixture bounds. The absorbed strain energy, *U*, corresponds to the area under the recorded stress-strain curves. (**C**) Measured stress-strain response of a 52/48 gyroid IPC compared to the corresponding rule-of-mixture prediction. (**D**) Characteristic nickel and carbon micropillar experiments showing the individual mechanical behavior of the IPC's two constituent materials. Scale bars, 5 μm.

50% brittle carbon, the IPC exhibited a ductile stress-strain response with an elongated ultrahigh-strength stress plateau extending until full compaction (Fig. 2C). Comparison with the rule-of-mixture response, which does not account for complex interaction between the two constituents, illustrates the contribution of the architecture in the mechanical efficiency of the IPC. Most notably, the interpenetrating design successfully prevented catastrophic fracture, which, in the rule of mixture, was associated with a pronounced stress drop. Simultaneously, the suppression of the reinforcement brittleness enabled ~1.5 GPa higher peak strength. A certain strength increase in the reinforcement shells with respect to the micropillars may also be attributed to their relatively smaller size, although available compression data on TPP-DLW–derived pyrolytic carbon (*37*–*39*) does not indicate a clear strengthening trend in the size regime below 5 μm. While nickel has a higher Young's modulus than pyrolytic carbon, *E* of the IPCs increased with the carbon content, with measured values being notably lower than the rule-of-mixture bound (Fig. 2B). However, Fig. 2C shows that this behavior was limited to small strains, where the linear response of the IPC was superimposed to a nonlinear toe. Stemming from slight sample-platen misalignment, this behavior commonly causes uncertainty and underestimation in Young's modulus measurements via compression (*38*). The effect intensified with increasing sample-platen contact areas, and toe regions became more pronounced as the specimen sizes increased with the nickel content. This may have caused the anomalous modulus increase with the carbon content. Other possible causes for the measured low values include weak bonding of the phase interfaces, as reported in previous IPC studies (*40*, *41*), and residual porosity within the specimens. More accurate Young's moduli can be determined via resonant frequency methods (*40*, *41*),

such as resonant ultrasound spectroscopy; however these techniques are challenging to implement at small scale.

We found spinodal reinforcements to be as efficient as gyroid surfaces, with no distinct difference in their measured properties. However, the possibility to synthesize the stochastic spinodal surfaces via self-assembly (*42*) may provide a pathway for the scalable manufacturing of nanoarchitected IPCs, representing a crucial advantage over periodic shell, beam, and plate architectures.

Our nanoarchitected nickel/carbon IPCs achieved unprecedented combination of compressive strength, strain energy absorption, and compressive deformability. Figure 3 compares our data to commercial bulk materials, as well as a large selection of literature-reported metal/ceramic and other architected IPCs, all of which have been characterized under uniaxial compression. The compared composites include additively manufactured polymer and metal IPCs with minimal surface shell designs and beam-lattice topologies, respectively; metal-dealloying–derived beam spinodal IPCs with individual ligaments as small as 15 nm (*43*); freeze cast nacre-like designs (*44*, *45*); biomorphic wood-based structures (*46*); and 3D woven fiber textiles (*47*, *48*). Figure 3A shows a compressive strength versus strain energy absorption chart, where our IPCs reach deep into the ultrahigh-strength and ultrahigh-energy white space, outperforming the compressive strength-to-energy absorption ratios of any bulk material, including cermets and hard metals such as tungsten carbides, which constitute some of the toughest state-of-the-art hard materials. The literature-reported IPCs are composed of much lighter matrix materials, such as aluminum and epoxy, and underperform the nanocomposites presented in this study by an order of magnitude or more. Many of these IPCs explicitly target high-performance lightweight applications, for which specific properties, i.e., property-to-density ratios, are most relevant. Figure 3B shows a specific compressive strength versus specific strain energy absorption chart. Beyond their superior absolute performance, our IPCs also drastically outperform the specific property ratios of other reported composites. Another measure for a material's resilience is its deformability, quantifiable by the maximum strain it can take while retaining load bearing capability. Figure 3C compares the maximum compressive strain and specific compressive strength of the literature-reported IPCs and our data. The former show a characteristic trade-off between strength and deformability, with the strongest materials being inherently brittle. In contrast, our IPCs achieved exceptional combinations of both high strength and deformability. The nanoarchitected metal/ceramic IPCs matched the large-strain deformability of low-strength metal and polymer IPCs while simultaneously exceeding the specific compressive strengths of strong yet brittle ceramics-based composites. This notably illustrates the efficacy of the introduced nanoscale minimal surface architecture. Many of the reported metal/ceramic IPCs are composed of similarly small-scale features as ours and reach comparable strengths. However, their imperfect architectures are consistent with limited deformability and orders of magnitude lower energy absorption capability.

To investigate the interdependency of composition, architecture, and achieved mechanical properties of nanoarchitected metal/ceramic IPCs, we compared our measurements to those of corresponding cellular carbon–only reinforcements. Figure 4 shows the stress-strain curves and deformation behaviors of our spinodal IPCs with nickel/carbon volume ratios of 81/19 and 57/43, alongside with previously reported cellular carbon spinodal shell nanolattices (*28*) with 19 and 43% relative density, $\bar{\rho}$, i.e., the solid material volume fraction. Carbon spinodal shell nanolattices with $\bar{\rho}$ of 19% and less have demonstrated that thin-walled minimal surface topologies grant a ductile-like layer-by-layer fracture mechanism despite the intrinsically brittle constituent materials. However, thicker shells cause early catastrophic shear fracture or vertical splitting, with minimal surface topologies alone being unable to maintain load-bearing

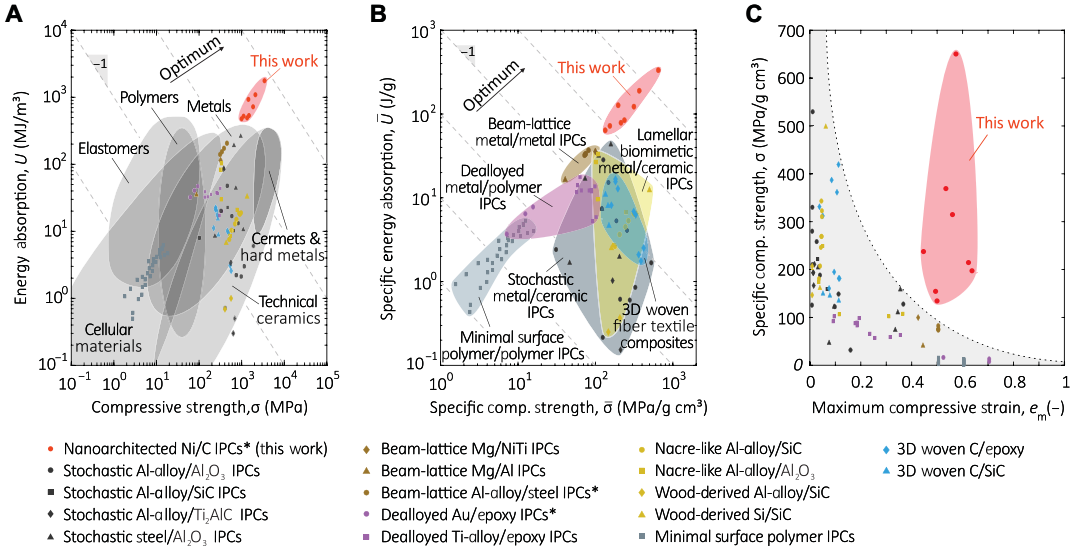

Fig. 3. Compressive strength, strain energy absorption, and deformability of nanoarchitected nickel/carbon IPCs compared to commercial bulk materials, literature-reported metal/ceramic IPCs, and other architected interpenetrating composites. Compressive strength versus strain energy absorption charts, (**A**) absolute and (**B**) specific properties, i.e., property-to-density ratios. The strain energy absorption values correspond to the areas under reported compressive stress-strain curves. (**C**) Specific strength versus maximum compressive strain chart. Data marked with asterisks (*) have not been tested to high-enough strains to reach fracture or densification. A reference list of the shown data is given in table S1.

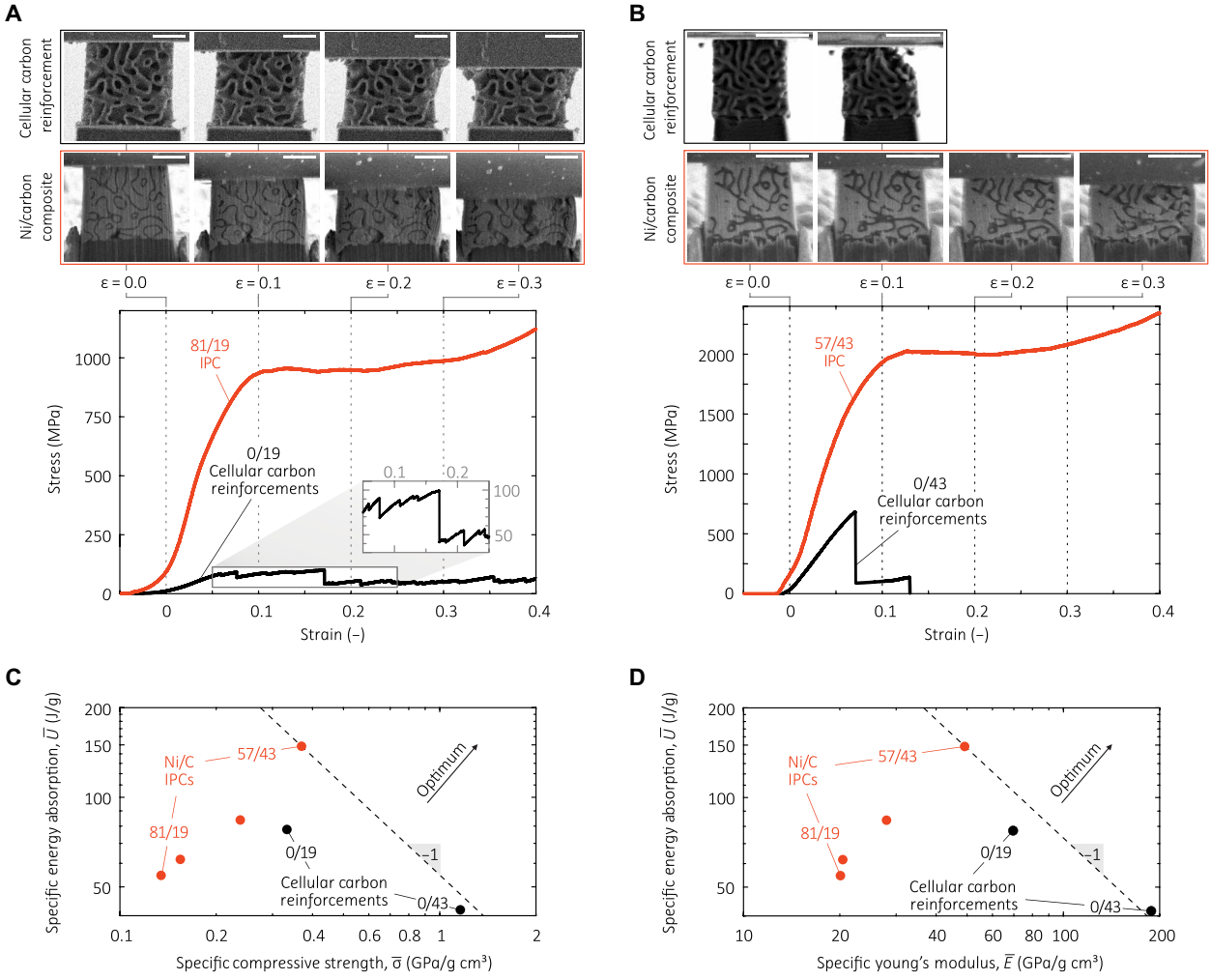

Fig. 4. Comparison of the mechanical behavior of nanoarchitected nickel/carbon IPCs with spinodal designs and their corresponding cellular carbon–only reinforcements. (**A** and **B**) Deformation behavior and stress-strain responses with thin- and thick-walled spinodal architectures, respectively. (**C** and **D**) Charts comparing specific strain energy absorption versus specific compressive strength and specific Young's modulus, respectively. Scale bars, 5 μm. Cellular carbon–only data were reproduced from (*28*).

capability in the postyield regime. In contrast to the cellular carbon–only reinforcements, all our IPCs achieved macroscopically plastic behaviors. Independent from the reinforcement content, the additional metal matrices granted the IPCs uniform, gradually barreling, deformability and the characteristic ductile stress-strain responses with elongated high-strength plateaus. There, the ceramic reinforcements largely remained contained by their metal matrices until full compaction, with some specimens undergoing gradual shear failure (fig. S3).

In situ image data revealed the beneficial deformation behavior of our IPCs related to toughening mechanisms on the scale of the individual nanofeatures. Movies S1 and S2 show confined plasticity of the nickel matrices to occur in proximity of localized fracture in the carbon phases. During such crack bridging events (*14*, *15*), plastically stretched metallic features act similar to small tensile specimens behind crack tips, exerting closure stresses that impede crack growth. Process zone shielding dissipates energy via plasticity and secondary cracking away from primary cracks. Dissipating additional energy, delamination and shearing of the nickel matrices against the carbon reinforcements can simultaneously be observed. However, this sliding mechanism also indicates relatively poor interface bonding, which can reduce the stiffness (*40*, *41*) and may have contributed to the low measured Young's moduli of the IPCs, as well as their apparent increase with the reinforcement content (Fig. 2B). In our specimens, only the carbon phases were constrained to the substrate. Considering that the interface area was similar in all IPCs, a given interface area had to constrain an increasing amount of material as the matrix volume ratio increased, resulting in a possible decrease of the resistance against interface sliding. With respect to all measured properties, interface strengthening approaches, such as incorporation of doping elements (*49*), may be a vital strategy to further improve the performance of nanoarchitected metal/ceramic IPCs.

DISCUSSION

Nanoarchitected IPCs are mechanically most efficient for designs allowing their constituents to contribute most antagonistic properties.

Here, the carbon reinforcements provided strength, while the nickel matrices suppressed the reinforcements' brittleness. Hence, the best combination of strength and strain energy absorption may be realized for the highest reinforcement content for which the matrix still prevents unstable crack propagation. Within low–reinforcement content metal/ceramic minimal surface IPCs, such as our 81/19 spinodal specimen, toughening mechanisms are limited to eliminating the reinforcement's serrated postyield response (see inset in Fig. 4A), as the thin-walled ceramic topologies already achieve ductile-like deformability. However, for high reinforcement contents, such as within the 57/43 spinodal IPC, the metal matrix efficiently suppresses catastrophic failure of its thick-walled reinforcement (Fig. 4B). Simultaneously, the 57/43 spinodal IPC's higher reinforcement content doubled the strength with respect to its 81/19 counterpart. While reinforcement contents were in this first study limited to below 50%, our data suggest that higher ratios may facilitate even better combinations of strength and strain energy absorption before properties ultimately approach those of the monolithic reinforcement. In this light, the designs of architected IPCs, which similarly to their cellular equivalents are generally derived from low-density lightweight topologies, may require some rethinking. The optimal design of high-density architectures is distinct from classical approaches (*50*) and has, so far, not received much attention. Our findings may provide valuable insights to spark the development of design methods of such materials.

Fully dense nanoarchitected metal/ceramic IPCs overcome the property trade-offs that currently limit the applicability of their cellular counterparts. The infiltration with metal matrices enables IPCs to drastically outperform their cellular-only reinforcements in any of the absolute mechanical properties (Fig. 4, A and B). With many cellular architected materials being very lightweight, though, a more intriguing comparison can be made by considering property-to-density ratios. Figure 4 (C and D) shows specific strain energy absorption, specific compressive strength, and specific Young's modulus of our spinodal IPCs and their cellular carbon–only reinforcements; an extended comparison including differently architected nanolattices is given in fig. S4. Their single-material design limits the cellular spinodal structures to leverage enhanced toughness via their architectural layout, which, in return, imposes a strength and stiffness trade-off. In contrast, the metal/ceramic composite design of our IPCs can be optimized to simultaneously maximize strength, stiffness, and strain energy absorption. Despite being mostly composed of heavy nickel matrices, the 57/43 spinodal IPC achieved better combinations of specific compressive strength and specific strain energy absorption than any of its cellular counterparts (Fig. 4C). Similarly, the IPC's ratio of specific Young's modulus to specific strain energy absorption was comparable to that of the stiffest cellular spinodal shell (Fig. 4D). Our IPCs outperformed all reported types of cellular architected materials, with the only exception being the recently introduced carbon plate nanolattices (fig. S4) (*51*). Furthermore, the properties reported here, particularly those normalized by the density, denote a lower bound. Given the limitations of the applied electrodeposition approach, the presence of residual porosity cannot be fully ruled out and the calculated densities represent the highest possible values. The incorporation of electrolyte additives has been reported to increase robustness in infiltrating high–aspect ratio structures (*35*) and could be adopted to improve the synthesis of nanoarchitected IPCs. It is also noted that our IPCs have, in contrast to their cellular counterparts, been exposed to FIB milling during fabrication, which can cause damage that may alter the mechanical properties at the specimen surface (*52*).

So far, the uncontested key attribute of cellular micro- and nanoarchitected materials has been their superior property-to-density ratios, which are of central relevance for the development of a novel generation of lightweight high-performance materials, for aerospace, energy, and transportation applications. Our findings now reveal that fully dense nanoarchitected IPCs do not only outperform their cellular counterparts in absolute terms but also rival their superiority for these weight-sensitive scenarios. While the main focus of this first proof-of-concept study did not cover weight efficiency, more advanced electrodeposition methods (*53*) could enable straightforward progression from heavy nickel matrices to lighter metals, such as aluminum. One may then easily expect similar performance as found here, with up to threefold higher specific properties.

Having demonstrated record compressive strength, strain energy absorption, and compressive deformability both in absolute and in specific terms, the nanoarchitected IPCs introduced in this work constitute a major advancement of the field of nanoarchitected materials, providing important groundwork for widespread research efforts across different disciplines throughout materials sciences. With each of the phases within interpenetrating composites having the ability to contribute radically distinct characteristics, the approach evolves the nanoarchitecture of materials from a strategy focused to achieve certain lightweight characteristics to a broadly applicable concept to design novel multifunctional systems, which may exploit a variety of unique nanoscale properties. The compressive characteristics demonstrated here are highly beneficial for impact protection, damping, and tribological and abrasive systems (*13*). In synergy with their mechanical performance, IPCs can be designed to exhibit properties such as high-temperature stability, superior thermal shock resistance, and high electrochemical cyclability (*13*, *54*). Regarding the mechanical performance of nanoarchitected metal/ceramic IPCs, it is emphasized that brittleness is typically most critical under tension. While the toughening mechanisms found here may be expected to be independent on the loading scenario, a detailed characterization of fracture toughness and tensile strength will be needed to quantify to which extent the superior compression behavior reported here translates to different load cases.

Novel nanoarchitected metal/ceramic IPCs may provide a pathway toward a host of unprecedented properties, with a potential application spectrum ranging from structural mechanics to thermal management and battery electrode materials (*13*). For this purpose, in particular, the investigated spinodal reinforcement architectures could be key. While the precisely controllable 3D printing route applied here granted the necessary reproducibility to validate the introduced IPC nanoarchitecture concept, it can currently not facilitate the scalability required for structural applications. Scalable manufacturing of nanoarchitected materials (including IPCs) is indeed an emerging area of active research. In particular, self-assembly of spinodal architectures (*32*, *33*) may be a manufacturing route able to retain the demonstrated beneficial properties in macroscopic structures. Recently reported centimeter-scale self-assembled cellular ceramic spinodal architectures (*42*), which are composed of nanometer-size shell features with comparable quality as the carbon reinforcements in this study, are a promising example. Mechanical data of first centimeter-size beam-based nano- and microlattices have demonstrated those to preserve the ultrahigh strength from

their nanoscale features across scales (*2*, *4*). Still, all scale-up approaches will face the challenge of circumventing the appearance of larger-range flaws, which would diminish properties with respect to the ones we have demonstrated here. Hence, comparison of nanoarchitected material specimens such as ours to existing bulk materials, as reported in Fig. 3, must be understood as a benchmark, denoting the performance that is potentially achievable from the nanoarchitecture approach.

MATERIALS AND METHODS

All IPCs were manufactured with pyrolytic carbon reinforcements and electrodeposited nickel matrices. First, reinforcement architecture templates were 3D printed on silicon substrates from the photoresist Ip-Dip (Nanoscribe GmbH) via TPP-DLW using a Photonic Professional GT (Nanoscribe GmbH). The TPP-DLW system was equipped with a Plan-Apochromat 63× 1.4 Oil DIC M27 objective (Carl Zeiss AG) and a FemtoFiber pro near-infrared pulsed laser (TOPTICA Photonics AG). After the TPP-DLW step, samples were submerged in propylene glycol monomethyl ether acetate (PGMEA) for 20 min to dissolve uncured photoresist, followed by a 5-min-long isopropanol bath to remove residual PGMEA. Samples were dried in an Autosamdri-931 critical point dryer (Tousimis Research Corp. Inc.) to circumvent collapse of the printed structures from surface tension during solvent evaporation. Specimens were then pyrolyzed into pyrolytic carbon at 900°C in a vacuum tube furnace following the recipe in (*6*). Subsequently, electrodeposition in a Watts bath for 25 min infiltrated the carbon reinforcements with nickel matrices. The used nickel anode had a purity of 99.9%, and the deposition was carried out at 20°C with a DC voltage of 2.5 V using a plating solution consisting of $NiSO_4$ $6H_2O$ (200 g/liter), Cl_2Ni $6H_2O$ (60 g/liter), and boric acid (50 g/liter). Last, FIB milling with an FEI Quanta 3D FEG dual beam (SEM/FIB) (Thermo Fisher Scientific Inc.) was used to cut the IPCs into cubical shape. The final specimens were free-standing cubes atop of pyrolytic carbon support pillars whose bottom face was attached to the silicon substrate. Likewise, monolithic micropillars were carved out of the nickel that had been electrodeposited on the silicon substrates. Pyrolytic carbon micropillars were TPP-DLW–printed and pyrolyzed under identical conditions as the IPC reinforcements.

Reinforcement and matrix feature dimensions of all IPCs were optically measured using a FEI Magellan 400XHR scanning electron microscope (SEM) (Thermo Fisher Scientific Inc.). With the SEM-measured dimensions, the nickel/carbon volume ratios of the IPCs were determined by computer-aided design (CAD) models. Specimen densities were determined with the literature-reported densities of pyrolytic carbon (*55*, *56*) and nickel (*57*) of 1.4 and 8.9 g/cm^3, respectively.

The mechanical behavior of the IPCs and the monolithic nickel and carbon micropillars were measured via uniaxial in situ compression at a constant strain rate of 0.01 s^{-1} inside a FEI Quanta 3D FEG dual beam (SEM/FIB) (Thermo Fisher Scientific Inc.), using an Alemnis Nanoindenter (Alemnis AG) equipped with a flat punch diamond tip. Load-displacement curves were recorded and corrected for instrument and substrate compliances with an in-house digital image correlation algorithm, which was tracking the specimen tops and bottoms. Engineering stress-strain curves were determined by applying the measured specimen dimensions. The Young's moduli, *E*, were measured as the maximum slopes of the curves' initial linear elastic regimes. The compressive strength, σ, corresponded to either the average plateau stress (*58*) between 20 and 40% strain or to an initial peak stress, whichever was higher. The strain energy absorption, *U*, was the area under the stress-strain curves. The *U* values in Figs. 2 and 4 were integrated from load onset to a cutoff strain of 44.175%. The cutoff strain was imposed by the experimental boundary conditions and corresponded to the lowest value of all applied maximum compressive strains of the IPCs, which ranged from 44 to 64%. The *U* values in Fig. 3 and fig. S4 were integrated from load onset to the individual maximum compressive strains. Notably, certain literature-reported *U* values in Fig. 3 and fig. S4 include substantially higher applied maximum strains than our data, meaning that the shown comparison provides a conservative estimate. None of our IPCs were testable to high-enough strains to reach a global energy absorption efficiency maximum (*59*), which defines the densification strain limit for *U* in cellular materials.

SUPPLEMENTARY MATERIALS

Supplementary material for this article is available at https://science.org/doi/10.1126/sciadv.abo3080

REFERENCES AND NOTES

1. J. Bauer, L. R. Meza, T. A. Schaedler, R. Schwaiger, X. Zheng, L. Valdevit, Nanolattices: An emerging class of mechanical metamaterials. *Adv. Mater.* **29**, 1701850 (2017).
2. X. Zheng, W. Smith, J. Jackson, B. Moran, H. Cui, D. Chen, J. Ye, N. Fang, N. Rodriguez, T. Weisgraber, C. M. Spadaccini, Multiscale metallic metamaterials. *Nat. Mater.* **15**, 1100–1106 (2016).
3. A. Vyatskikh, S. Delalande, A. Kudo, X. Zhang, C. M. Portela, J. R. Greer, Additive manufacturing of 3D nano-architected metals. *Nat. Commun.* **9**, 593 (2018).
4. Z. Jiang, J. H. Pikul, Centimetre-scale crack-free self-assembly for ultra-high tensile strength metallic nanolattices. *Nat. Mater.* **20**, 1512–1518 (2021).
5. L. R. Meza, S. Das, J. R. Greer, Strong, lightweight, and recoverable three-dimensional ceramic nanolattices. *Science* **345**, 1322–1326 (2014).
6. J. Bauer, A. Schroer, R. Schwaiger, O. Kraft, Approaching theoretical strength in glassy carbon nanolattices. *Nat. Mater.* **15**, 438–443 (2016).
7. J. Bauer, C. Crook, A. Guell Izard, Z. C. Eckel, N. Ruvalcaba, T. A. Schaedler, L. Valdevit, Additive manufacturing of ductile, ultrastrong polymer-derived nanoceramics. *Matter* **1**, 1547–1556 (2019).
8. J. Ye, L. Liu, J. Oakdale, J. Lefebvre, S. Bhowmick, T. Voisin, J. D. Roehling, W. L. Smith, M. R. Cerón, J. van Ham, L. B. Bayu Aji, M. M. Biener, Y. M. Wang, P. R. Onck, J. Biener, Ultra-low-density digitally architected carbon with a strutted tube-in-tube structure. *Nat. Mater.* **20**, 1498–1505 (2021).
9. N. P. Padture, Advanced structural ceramics in aerospace propulsion. *Nat. Mater.* **15**, 804–809 (2016).
10. R. Velu, T. Calais, A. Jayakumar, F. Raspall, A comprehensive review on bio-nanomaterials for medical implants and feasibility studies on fabrication of such implants by additive manufacturing technique. *Materials (Basel)* **13**, 92 (2020).
11. K. K. Chawla, *Composite Materials: Science and Engineering* (Springer, ed. 3, 2012).
12. D. R. Clarke, Interpenetrating phase composites. *J. Am. Ceram. Soc.* **75**, 739–758 (1992).
13. N. Kota, M. S. Charan, T. Laha, S. Roy, Review on development of metal/ceramic interpenetrating phase composites and critical analysis of their properties. *Ceram. Int.* **48**, 1451–1483 (2021).
14. H. Prielipp, M. Knechtel, N. Claussen, S. K. Streiffer, H. Müllejans, M. Rühle, J. Rödel, Strength and fracture toughness of aluminum/alumina composites with interpenetrating networks. *Mater. Sci. Eng. A* **197**, 19–30 (1995).
15. L. D. Wegner, L. J. Gibson, The fracture toughness behaviour of interpenetrating phase composites. *Int. J. Mech. Sci.* **43**, 1771–1791 (2001).
16. P. Agrawal, C. T. Sun, Fracture in metal–ceramic composites. *Compos. Sci. Technol.* **64**, 1167–1178 (2004).
17. M. Kouzeli, D. C. Dunand, Effect of reinforcement connectivity on the elasto-plastic behavior of aluminum composites containing sub-micron alumina particles. *Acta Mater.* **51**, 6105–6121 (2003).
18. L. D. Wegner, L. J. Gibson, The mechanical behaviour of interpenetrating phase composites - I: Modelling. *Int. J. Mech. Sci.* **42**, 925–942 (2000).
19. L. Wang, J. Lau, E. L. Thomas, M. C. Boyce, Co-continuous composite materials for stiffness, strength, and energy dissipation. *Adv. Mater.* **23**, 1524–1529 (2011).
20. T. Li, Y. Chen, L. Wang, Enhanced fracture toughness in architected interpenetrating phase composites by 3D printing. *Compos. Sci. Technol.* **167**, 251–259 (2018).

21. O. Al-Ketan, M. Adel Assad, R. K. Abu Al-Rub, Mechanical properties of periodic interpenetrating phase composites with novel architected microstructures. *Compos. Struct.* **176**, 9–19 (2017).
22. O. Al-Ketan, R. K. A. Al-Rub, R. Rowshan, Mechanical properties of a new type of architected interpenetrating phase composite materials. *Adv. Mater. Technol.* **2**, 1600235 (2017).
23. Y. Zhang, M. T. Hsieh, L. Valdevit, Mechanical performance of 3D printed interpenetrating phase composites with spinodal topologies. *Compos. Struct.* **263**, 113693 (2021).
24. C. San Marchi, M. Kouzeli, R. Rao, J. A. Lewis, D. C. Dunand, Alumina-aluminum interpenetrating-phase composites with three-dimensional periodic architecture. *Scr. Mater.* **49**, 861–866 (2003).
25. R. Soundararajan, G. Kuhn, R. Atisivan, S. Bose, A. Bandyopadhyay, Processing of mullite–aluminum composites. *J. Am. Ceram. Soc.* **84**, 509–513 (2001).
26. A. S. Dalaq, D. W. Abueidda, R. K. Abu Al-Rub, Mechanical properties of 3D printed interpenetrating phase composites with novel architectured 3D solid-sheet reinforcements. *Compos. Part A Appl. Sci. Manuf.* **84**, 266–280 (2016).
27. M.-T. Hsieh, B. Endo, Y. Zhang, J. Bauer, L. Valdevit, The mechanical response of cellular materials with spinodal topologies. *J. Mech. Phys. Solids* **125**, 401–419 (2019).
28. A. Guell Izard, J. Bauer, C. Crook, V. Turlo, L. Valdevit, Ultrahigh energy absorption multifunctional spinodal nanoarchitectures. *Small* **15**, 1903834 (2019).
29. A. Vidyasagar, S. Krödel, D. M. Kochmann, Microstructural patterns with tunable mechanical anisotropy obtained by simulating anisotropic spinodal decomposition. *Proc. R. Soc. A Math. Phys. Eng. Sci.* **474**, 20180535 (2018).
30. J. W. Cahn, On spinodal decomposition. *Acta Metall.* **9**, 795–801 (1961).
31. H. Jinnai, T. Koga, Y. Nishikawa, T. Hashimoto, S. T. Hyde, Curvature determination of spinodal interface in a condensed matter system. *Phys. Rev. Lett.* **78**, 2248–2251 (1997).
32. M. N. Lee, A. Mohraz, Bicontinuous macroporous materials from Bijel templates. *Adv. Mater.* **22**, 4836–4841 (2010).
33. S. Ndoni, M. E. Vigild, R. H. Berg, Nanoporous materials with spherical and gyroid cavities created by quantitative etching of polydimethylsiloxane in polystyrene–polydimethylsiloxane block copolymers. *J. Am. Chem. Soc.* **125**, 13366–13367 (2003).
34. K. E. Pappacena, M. T. Johnson, S. Xie, K. T. Faber, Processing of wood-derived copper–silicon carbide composites via electrodeposition. *Compos. Sci. Technol.* **70**, 485–491 (2010).
35. M. T. Johnson, A. S. Childers, F. De Carlo, X. Xiao, K. T. Faber, Wood-derived copper–graphite composites produced via additive-assisted electrodeposition. *Compos. Sci. Technol.* **89**, 61–68 (2013).
36. X. W. Gu, J. R. Greer, Ultra-strong architected Cu meso-lattices. *Extrem. Mech. Lett.* **2**, 7–14 (2015).
37. A. Albiez, R. Schwaiger, Size effect on the strength and deformation behavior of glassy carbon nanopillars. *MRS Adv.* **4**, 133–138 (2019).
38. X. Zhang, L. Zhong, A. Mateos, A. Kudo, A. Vyatskikh, H. Gao, J. R. Greer, X. Li, Theoretical strength and rubber-like behaviour in micro-sized pyrolytic carbon. *Nat. Nanotechnol.* **14**, 762–769 (2019).
39. E. Rossi, J. Bauer, M. Sebastiani, Humidity-dependent flaw sensitivity in the crack propagation resistance of 3d-printed nano-ceramics. *Scr. Mater.* **194**, 113684 (2021).
40. I. V. Okulov, P.-A. Geslin, I. V. Soldatov, H. Ovri, S. H. Joo, H. Kato, Anomalously low modulus of the interpenetrating-phase composite of Fe and Mg obtained by liquid metal dealloying. *Scr. Mater.* **163**, 133–136 (2019).
41. I. V. Okulov, J. Wilmers, S.-H. Joo, S. Bargmann, H. S. Kim, H. Kato, Anomalous compliance of interpenetrating-phase composite of Ti and Mg synthesized by liquid metal dealloying. *Scr. Mater.* **194**, 113660 (2021).
42. C. M. Portela, A. Vidyasagar, S. Krödel, T. Weissenbach, D. W. Yee, J. R. Greer, D. M. Kochmann, Extreme mechanical resilience of self-assembled nanolabyrinthine materials. *Proc. Natl. Acad. Sci. U.S.A.* **117**, 5686–5693 (2020).
43. K. Wang, J. Weissmüller, Composites of nanoporous gold and polymer. *Adv. Mater.* **25**, 1280–1284 (2013).
44. R. O. Ritchie, The conflicts between strength and toughness. *Nat. Mater.* **10**, 817–822 (2011).
45. W. Huang, D. Restrepo, J.-Y. Jung, F. Y. Su, Z. Liu, R. O. Ritchie, J. McKittrick, P. Zavattieri, D. Kisailus, Multiscale toughening mechanisms in biological materials and bioinspired designs. *Adv. Mater.* **31**, 1901561 (2019).
46. M. Yu, G.-j. Zhang, T. Saunders, Wood-derived ultra-high temperature carbides and their composites: A review. *Ceram. Int.* **46**, 5536–5547 (2020).
47. A. P. Mouritz, M. K. Bannister, P. J. Falzon, K. H. Leong, Review of applications for advanced three-dimensional fibre textile composites. *Compos. Part A Appl. Sci. Manuf.* **30**, 1445–1461 (1999).
48. T. Huang, Y. Wang, G. Wang, Review of the mechanical properties of a 3D woven composite and its applications. *Polym. Plast. Technol. Eng.* **57**, 740–756 (2017).
49. Y. Chen, X. Liu, T. Zhang, H. Xie, N. Zhao, C. Shi, C. He, J. Li, E. Liu, Interface intrinsic strengthening mechanism on the tensile properties of Al_2O_3/Al composites. *Comput. Mater. Sci.* **169**, 109131 (2019).
50. B. Deng, G. J. Cheng, Soap film inspired mechanical metamaterials approaching theoretical bound of stiffness across full density range. *Mater. Horizons* **8**, 987–996 (2021).
51. C. Crook, J. Bauer, A. Guell Izard, C. Santos de Oliveira, J. Martins de Souza e Silva, J. B. Berger, L. Valdevit, Plate-nanolattices at the theoretical limit of stiffness and strength. *Nat. Commun.* **11**, 1579 (2020).
52. C. A. Volkert, A. M. Minor, Focused ion beam microscopy and micromachining. *MRS Bull.* **32**, 389–399 (2007).
53. K. K. Maniam, S. Paul, A review on the electrodeposition of aluminum and aluminum alloys in ionic liquids. *Coatings* **11**, 80 (2021).
54. J. Wu, Z. Zhu, H. Zhang, H. Fu, H. Li, A. Wang, H. Zhang, Z. Hu, A novel nano-structured interpenetrating phase composite of silicon/graphite-tin for lithium-ion rechargeable batteries anode materials. *J. Alloys Compd.* **596**, 86–91 (2014).
55. F. C. Cowlard, J. C. Lewis, Vitreous carbon—A new form of carbon. *J. Mater. Sci.* **2**, 507–512 (1967).
56. O. J. A. Schueller, S. T. Brittain, C. Marzolin, G. M. Whitesides, Fabrication and characterization of glassy carbon MEMS. *Chem. Mater.* **9**, 1399–1406 (1997).
57. L. J. Gibson, M. F. Ashby, *Cellular Solids: Structure and Properties* (Cambridge Univ. Press, ed. 2, 2001).
58. M. O. Normalizacyjna, Mechanical testing of metals - Ductility testing - Compression test for porous and cellular metals ISO 13314 (ISO, Geneva, 2011).
59. Q. M. Li, I. Magkiriadis, J. J. Harrigan, Compressive strain at the onset of densification of cellular solids. *J. Cell. Plast.* **42**, 371–392 (2006).
60. D. M. Dimiduk, M. D. Uchic, T. A. Parthasarathy, Size-affected single-slip behavior of pure nickel microcrystals. *Acta Mater.* **53**, 4065–4077 (2005).
61. M. D. Uchic, P. A. Shade, D. M. Dimiduk, Plasticity of micrometer-scale single crystals in compression. *Annu. Rev. Mat. Res.* **39**, 361–386 (2009).
62. C. P. Frick, B. G. Clark, S. Orso, A. S. Schneider, E. Arzt, Size effect on strength and strain hardening of small-scale [111] nickel compression pillars. *Mater. Sci. Eng. A* **489**, 319–329 (2008).
63. B. B. Seo, J. Gu, Z. Jahed, T. Y. Tsui, Influence of grain boundary modifier on the strength size-dependence displayed by complex-shaped nanocrystalline nickel pillars. *Thin Solid Films* **621**, 178–183 (2017).
64. J. R. Greer, J. T. M. De Hosson, Plasticity in small-sized metallic systems: Intrinsic versus extrinsic size effect. *Prog. Mater. Sci.* **56**, 654–724 (2011).
65. J. K. Luo, A. J. Flewitt, S. M. Spearing, N. A. Fleck, W. I. Milne, Young's modulus of electroplated Ni thin film for MEMS applications. *Mater. Lett.* **58**, 2306–2309 (2004).
66. T. H. Courtney, *Mechanical Behavior of Materials* (Waveland Press, ed. 2, 2005).
67. A. Rajpurohit, S. Joannès, V. Singery, P. Sanial, L. Laiarinandrasana, Hybrid effect in in-plane loading of carbon/glass fibre based inter- and intraply hybrid composites. *J. Compos. Sci.* **4**, 6 (2020).
68. X. Zhang, A. Vyatskikh, H. Gao, J. R. Greer, X. Li, Lightweight, flaw-tolerant, and ultrastrong nanoarchitected carbon. *Proc. Natl. Acad. Sci. U.S.A.* **116**, 6665–6672 (2019).
69. X. Zheng, H. Lee, T. H. Weisgraber, M. Shusteff, J. DeOtte, E. B. Duoss, J. D. Kuntz, M. M. Biener, Q. Ge, J. A. Jackson, S. O. Kucheyev, N. X. Fang, C. M. Spadaccini, Ultralight, ultrastiff mechanical metamaterials. *Science* **344**, 1373–1377 (2014).
70. T. A. Schaedler, A. J. Jacobsen, A. Torrents, A. E. Sorensen, J. Lian, J. R. Greer, L. Valdevit, W. B. Carter, Ultralight metallic microlattices. *Science* **334**, 962–965 (2011).
71. L. Salari-Sharif, T. A. Schaedler, L. Valdevit, Energy dissipation mechanisms in hollow metallic microlattices. *J. Mater. Res.* **29**, 1755–1770 (2014).
72. J. H. Pikul, S. Özerinç, B. Liu, R. Zhang, P. V. Braun, V. S. Deshpande, W. P. King, High strength metallic wood from nanostructured nickel inverse opal materials. *Sci. Rep.* **9**, 719 (2019).
73. L. Zhang, S. Feih, S. Daynes, S. Chang, M. Y. Wang, J. Wei, W. F. Lu, Energy absorption characteristics of metallic triply periodic minimal surface sheet structures under compressive loading. *Addit. Manuf.* **23**, 505–515 (2018).
74. S. Yin, W. Guo, H. Wang, Y. Huang, R. Yang, Z. Hu, D. Chen, J. Xu, R. O. Ritchie, Strong and tough bioinspired additive-manufactured dual-phase mechanical metamaterial composites. *J. Mech. Phys. Solids* **149**, 104341 (2021).
75. C. A. Volkert, E. T. Lilleodden, D. Kramer, J. Weissmüller, Approaching the theoretical strength in nanoporous Au. *Appl. Phys. Lett.* **89**, 061920 (2006).
76. J. Biener, A. M. Hodge, J. R. Hayes, C. A. Volkert, L. A. Zepeda-ruiz, A. V Hamza, F. F. Abraham, Size effects on the mechanical behavior of nanoporous Au. *Nano Lett.* **6**, 2379–2382 (2006).
77. I. V. Okulov, J. Weissmüller, J. Markmann, Dealloying-based interpenetrating-phase nanocomposites matching the elastic behavior of human bone. *Sci. Rep.* **7**, 20 (2017).
78. J. Bauer, S. Hengsbach, I. Tesari, R. Schwaiger, O. Kraft, High-strength cellular ceramic composites with 3D microarchitecture. *Proc. Natl. Acad. Sci. U.S.A.* **111**, 2453–2458 (2014).
79. J. Bauer, A. Schroer, R. Schwaiger, O. Kraft, The impact of size and loading direction on the strength of architected lattice materials. *Adv. Eng. Mater.* **18**, 1537–1543 (2016).
80. M. Mieszala, M. Hasegawa, G. Guillonneau, J. Bauer, R. Raghavan, C. Frantz, O. Kraft, S. Mischler, J. Michler, L. Philippe, Micromechanics of amorphous metal/polymer hybrid

structures with 3D cellular architectures: Size effects, buckling behavior, and energy absorption capability. *Small* **13**, 1602514 (2017).
81. J. J. do Rosário, J. B. Berger, E. T. Lilleodden, R. M. McMeeking, G. A. Schneider, The stiffness and strength of metamaterials based on the inverse opal architecture. *Extrem. Mech. Lett.* **12**, 86–96 (2016).
82. L. Xu, thesis, The Ohio State University (1994).
83. F. Scherm, R. Völkl, A. Neubrand, F. Bosbach, U. Glatzel, Mechanical characterisation of interpenetrating network metal–ceramic composites. *Mater. Sci. Eng. A* **527**, 1260–1265 (2010).
84. J. Schukraft, C. Lohr, K. A. Weidenmann, 2D and 3D in-situ mechanical testing of an interpenetrating metal ceramic composite consisting of a slurry-based ceramic foam and AlSi10Mg. *Compos. Struct.* **263**, 113742 (2021).
85. M. K. Aghajanian, N. H. MacMillan, C. R. Kennedy, S. J. Luszcz, R. Roy, Properties and microstructures of Lanxide® Al_2O_3-Al ceramic composite materials. *J. Mater. Sci.* **24**, 658–670 (1989).
86. W. Liu, U. Köster, Microstructures and properties of interpenetrating alumina/aluminium composites made by reaction of SiO_2 glass preforms with molten aluminium. *Mater. Sci. Eng. A* **210**, 1–7 (1996).
87. M. Potoczek, R. E. Sliwa, Microstructure and physical properties of $AlMg/Al_2O_3$ interpenetrating composites fabricated by metal infiltration into ceramic foams. *Arch. Metall. Mater.* **56**, 1265–1269 (2011).
88. B. Mummareddy, M. Maravola, E. MacDonald, J. Walker, B. Hetzel, B. Conner, P. Cortes, The fracture properties of metal-ceramic composites manufactured via stereolithography. *Int. J. Appl. Ceram. Technol.* **17**, 413–423 (2020).
89. L.-Z. Zhao, M.-J. Zhao, H. Yan, X.-M. Cao, J.-S. Zhang, Mechanical behavior of SiC foam-SiC particles/Al hybrid composites. *Trans. Nonferrous Met. Soc. China* **19**, s547–s551 (2009).
90. D. A. H. Hanaor, L. Hu, W. H. Kan, G. Proust, M. Foley, I. Karaman, M. Radovic, Compressive performance and crack propagation in Al alloy/Ti_2AlC composites. *Mater. Sci. Eng. A* **672**, 247–256 (2016).
91. L. Hu, A. Kothalkar, M. O'Neil, I. Karaman, M. Radovic, Current-activated, pressure-assisted infiltration: A novel, versatile route for producing interpenetrating ceramic–metal composites. *Mater. Res. Lett.* **2**, 124–130 (2014).
92. S. B. Hein, Powder injection moulding of metal ceramic interpenetrating phase composites. *Powder Metall.* **57**, 348–356 (2014).
93. M. Zhang, Q. Yu, Z. Liu, J. Zhang, D. Jiao, S. Li, H. Peng, Q. Wang, Z. Zhang, R. O. Ritchie, Compressive properties of 3-D printed Mg–NiTi interpenetrating-phase composite: Effects of strain rate and temperature. *Compos. Part B Eng.* **215**, 108783 (2021).
94. M. Zhang, Q. Yu, Z. Liu, J. Zhang, G. Tan, D. Jiao, W. Zhu, S. Li, Z. Zhang, R. Yang, R. O. Ritchie, 3D printed Mg-NiTi interpenetrating-phase composites with high strength, damping capacity, and energy absorption efficiency. *Sci. Adv.* **6**, eaba5581 (2020).
95. H. Wang, M. Su, H. Hao, Compressive properties and energy absorption behavior of $Mg_{17}Al_{12}$/Al ordered structure composites. *Compos. Part B Eng.* **210**, 108688 (2021).
96. A. E. Pawlowski, Z. C. Cordero, M. R. French, T. R. Muth, J. Keith Carver, R. B. Dinwiddie, A. M. Elliott, A. Shyam, D. A. Splitter, Damage-tolerant metallic composites via melt infiltration of additively manufactured preforms. *Mater. Des.* **127**, 346–351 (2017).
97. A. Shaga, P. Shen, C. Sun, Q. Jiang, Lamellar-interpenetrated Al–Si–Mg/SiC composites fabricated by freeze casting and pressureless infiltration. *Mater. Sci. Eng. A* **630**, 78–84 (2015).
98. A. Shaga, P. Shen, R. F. Guo, Q.-C. Jiang, Effects of oxide addition on the microstructure and mechanical properties of lamellar SiC scaffolds and Al–Si–Mg/SiC composites prepared by freeze casting and pressureless infiltration. *Ceram. Int.* **42**, 9653–9659 (2016).
99. S. Roy, B. Butz, A. Wanner, Damage evolution and domain-level anisotropy in metal/ceramic composites exhibiting lamellar microstructures. *Acta Mater.* **58**, 2300–2312 (2010).
100. T. E. Wilkes, M. L. Young, R. E. Sepulveda, D. C. Dunand, K. T. Faber, Composites by aluminum infiltration of porous silicon carbide derived from wood precursors. *Scr. Mater.* **55**, 1083–1086 (2006).
101. J. Martínez-Fernández, F. M. Valera-Feria, M. Singh, High temperature compressive mechanical behavior of biomorphic silicon carbide ceramics. *Scr. Mater.* **43**, 813–818 (2000).
102. W.-S. Kuo, T.-H. Ko, C.-P. Chen, Effect of weaving processes on compressive behavior of 3D woven composites. *Compos. Part A Appl. Sci. Manuf.* **38**, 555–565 (2007).
103. B. N. Cox, M. S. Dadkhah, W. L. Morris, J. G. Flintoff, Failure mechanisms of 3D woven composites in tension, compression, and bending. *Acta Metall. Mater.* **42**, 3967–3984 (1994).
104. T. Suo, X. Fan, G. Hu, Y. Li, Z. Tang, P. Xue, Compressive behavior of C/SiC composites over a wide range of strain rates and temperatures. *Carbon* **62**, 481–492 (2013).

Acknowledgments: SEM imaging and in situ mechanical testing were performed at the UC Irvine Materials Research Institute (IMRI). We are thankful to A. Guell Izard, who provided CAD files and SEM images for the carbon spinodal shells. **Funding:** This work was financially supported by the Office of Naval Research (program manager: D. Shifler; grant no. N00014-17-1-2874) and the Army Research Laboratory (contract no. W911NF-15-2-0024; via a subcontract from Worcester Polytechnic Institute). **Author contributions:** L.V. conceived the research. M.S.-C., J.B., and M.A. manufactured specimens. M.S.-C., J.B., and M.A. conducted experimental characterizations. M.S.-C. and J.B. analyzed the experimental data. M.S.-C., J.B., and L.V. interpreted results, and M.S.-C. and J.B. wrote the manuscript. **Competing interests:** The authors declare that they have no competing interests. **Data and materials availability:** All data needed to evaluate the conclusions in the paper are present in the paper and/or the Supplementary Materials.

Submitted 26 January 2022
Accepted 6 July 2022
Published 17 August 2022
10.1126/sciadv.abo3080